PNAS
www.pnas.org

Supplementary Information for

Imaging the dynamic recruitment of monocytes to the blood-brain barrier and specific brain regions during *Toxoplasma gondii* infection

Christine A. Schneider, Dario X. Figueroa Velez, Ricardo Azevedo, Evelyn M. Hoover, Cuong Joseph Tran, Chelsie Lo, Omid Vadpey, Sunil P. Gandhi, and Melissa B. Lodoen

Corresponding author: Melissa B. Lodoen

Email: mlodoen@uci.edu

This PDF file includes:

Figures S1 to S7
Tables S1 to S5
Captions for movies S1 to S3
Supplementary Materials & Methods

Other supplementary materials for this manuscript include the following:

Movies S1 to S3

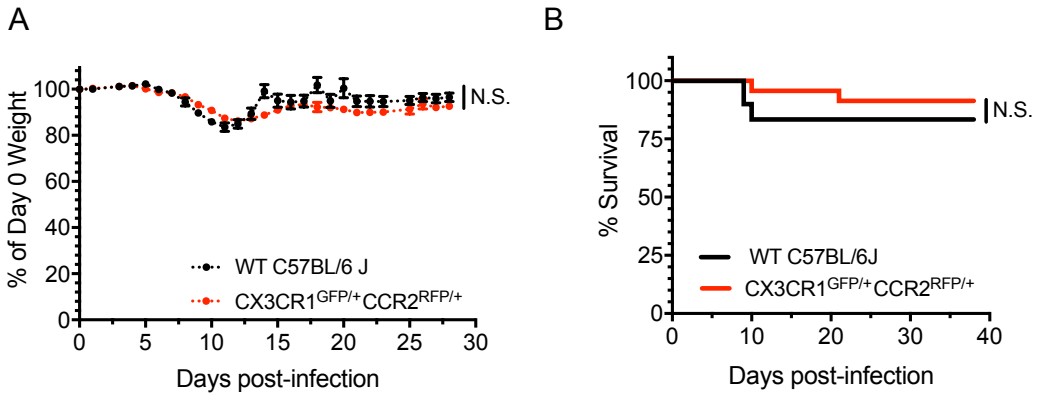

Fig. S1. Weight loss and survival of CCR2$^{RFP/+}$CX3CR1$^{GFP/+}$ mice infected with *T. gondii.* Wild-type (WT) C57BL/6J mice and CCR2$^{RFP/+}$CX3CR1$^{GFP/+}$ mice were infected with 200 type II *T. gondii* tachyzoites. **A)** Mice were monitored for weight loss. Weight loss curves were not significantly different between genotypes when compared by linear regression and were not significantly different at endpoint by Student's *t* test. **B)** Kaplan-Meier survival curves were generated. $n_{WT} = 8$, $n_{CCR2^{RFP/+}CX3CR1^{GFP/+}} = 13$.

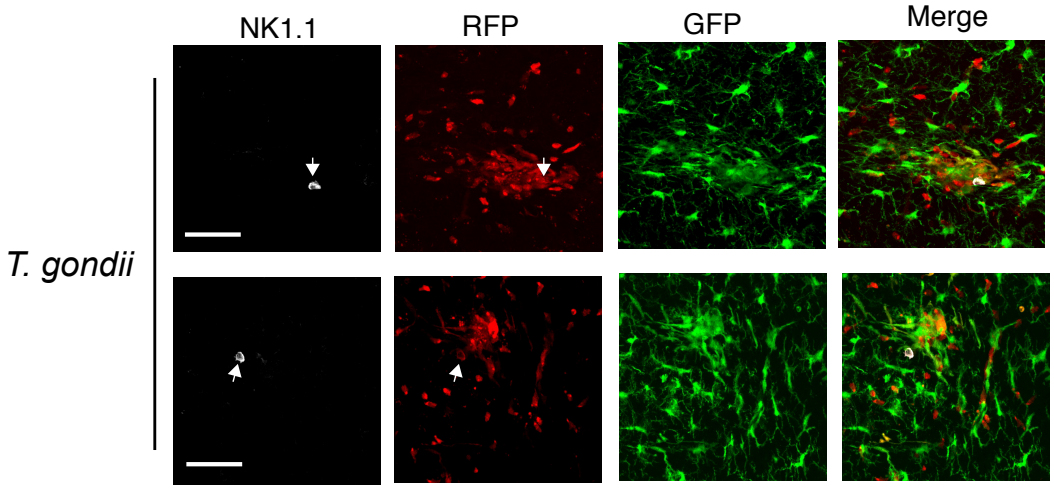

Fig. S2. Rare detection of CCR2-RFP cells expressing the NK cell marker NK1.1 in the brain. Brain sections from $CCR2^{RFP/+}CX3CR1^{GFP/+}$ mice infected with *T. gondii* were stained with antibody against NK1.1 and visualized by confocal microscopy. Arrows indicate cells positive for $NK1.1^{+}$ staining. Scale bars = 50 μm.

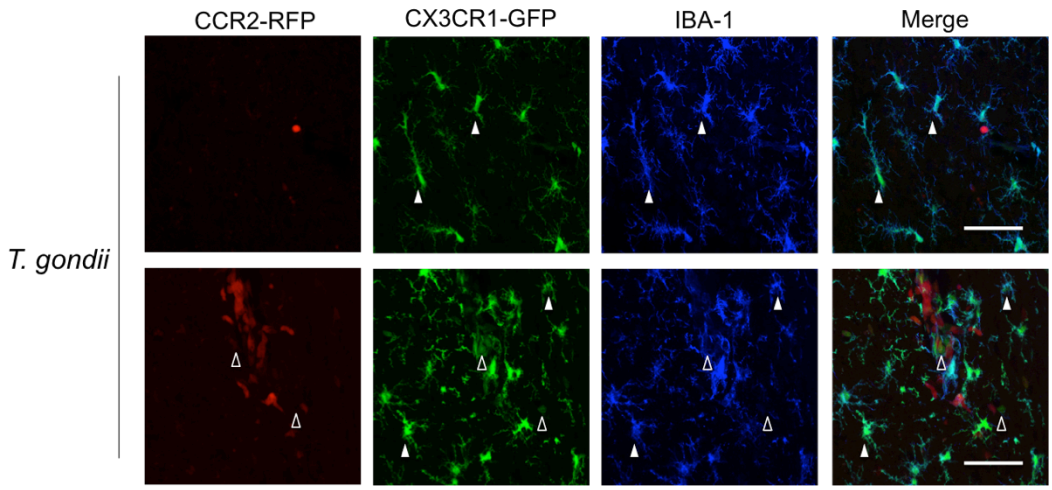

Fig. S3. GFP^{hi} cells are IBA-1^{+}. Brain sections from CCR2$^{RFP/+}$CX3CR1$^{GFP/+}$ mice infected with *T. gondii* were stained with antibody against IBA-1 and visualized by confocal microscopy. Filled arrowheads indicate CX3CR1-GFP^{hi} cells that are also positive for IBA-1 staining. Open arrowheads indicate CX3CR1-GFP^{lo}, IBA-1^{-} cells. Scale bars = 50 μm.

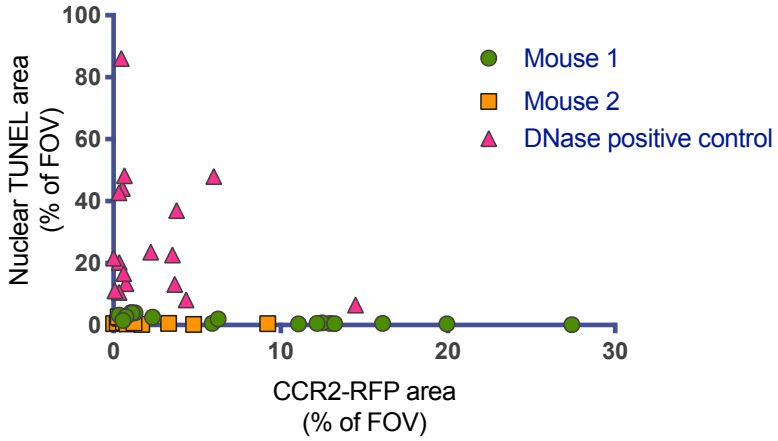

Fig. S4. Cell apoptosis is not increased in regions of increased monocyte density in the brain. Brain sections from CCR2$^{RFP/+}$CX3CR1$^{GFP/+}$ mice infected with *T. gondii* were stained for DNA damage using TUNEL and compared to CCR2-RFP signal in the same field of view. Percent of the field containing RFP signal was plotted against the percent of thresholded nucleus area containing positive staining for DNA strand breaks. Separate brain sections from the same mice were incubated with DNase as a positive control and quantified in the same way.

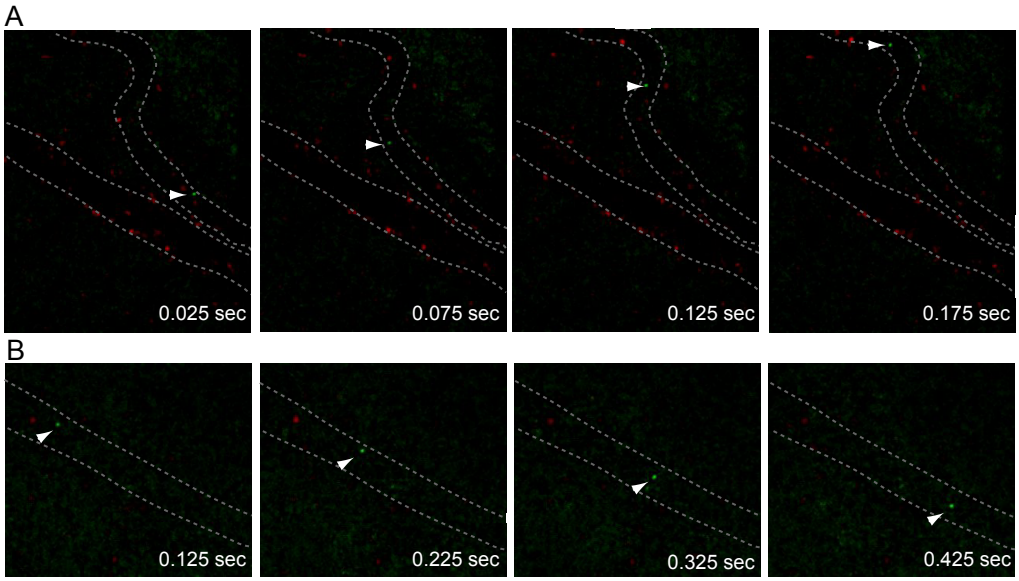

Fig. S5. GFP$^+$ *T. gondii* are detectable by 2-photon microscopy. A CCR2$^{RFP/+}$ mouse was injected I.V. with *T. gondii,* and the brain was imaged through a cranial window using 2-photon microscopy. Two separate fields of view are shown in **(A)** and **(B)**. Arrowheads indicate GFP$^+$ parasites travelling through blood vessels, and the borders of the vessels were outlined with dotted lines.

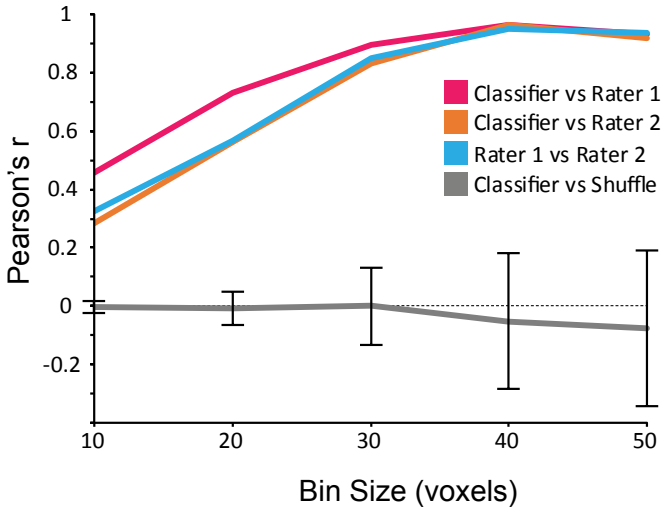

Fig. S6. Validation of segmentation algorithm for CCR2-RFP cells in optically-cleared brains. A representative substack of imaging data from a *T. gondii*-infected mouse at 15 dpi was quantified for CCR2-RFP cells by the classifier (segmentation pipeline) and by two independent human raters. Detected cells were spatially binned in 3D, and Pearson's *r* was calculated between raters for several bin sizes.

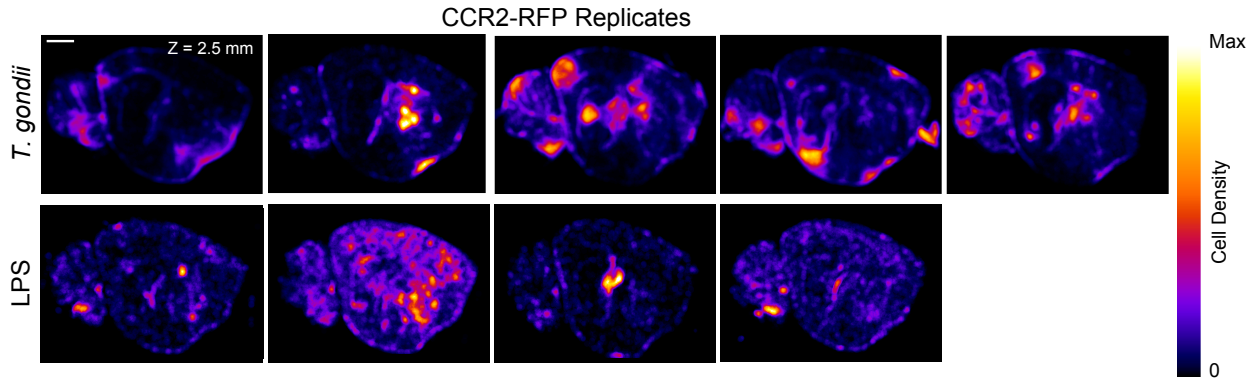

Fig. S7. Individual heatmaps of monocyte density from mice injected with LPS or *T. gondii*. CCR2$^{RFP/+}$ mice were injected with *T. gondii* or LPS, and the brains were harvested for optical clearing and lightsheet microscopy. The heatmaps of CCR2-RFP monocyte signal from each brain are shown. The mean heatmaps showing the combined data from all the mice in each condition are depicted in Figure 8A.

Table S1. CD45$^+$ cell frequencies in the blood of control (PBS) or *T. gondii*-infected mice.

	T cells	B cells	PMN	NKT cells	NK cells	Monocytes	CD11c	Others
PBS (early)	23.22 ± 1.95	66.62 ± 2.01	0.63 ± 0.13	0.5 ± 0.14	3.61 ± 0.59	1.07 ± 0.2	2.23 ± 0.56	1.81 ± 0.24
4 DPI	35.14 ± 2.55	43.67 ± 3.22	0.99 ± 0.31	0.52 ± 0.09	8.18 ± 0.87	3.27 ± 0.48	4.21 ± 0.95	4.33 ± 0.47
6 DPI	25.45 ± 4	29.08 ± 2.87	4.2 ± 1.19	1.82 ± 0.71	14.88 ± 1.64	3.52 ± 0.37	10.02 ± 1.67	11.91 ± 3.41
PBS (late)	29.58 ± 0.66	61.65 ± 1.67	0.27 ± 0.05	0.36 ± 0.02	2.29 ± 0.25	0.86 ± 0.09	1.35 ± 0.16	3.64 ± 0.89
10 DPI	45.32 ± 4.66	17.73 ± 4.67	1.1 ± 0.19	2.02 ± 0.11	9.54 ± 1.79	1.62 ± 0.19	8.78 ± 1.85	13.89 ± 1.12
15 DPI	55.13 ± 1.28	17.33 ± 2.8	3.6 ± 0.91	3.97 ± 0.4	6.12 ± 0.79	1.31 ± 0.33	3.3 ± 0.65	9.24 ± 2
38 DPI	31.24 ± 1.81	59.64 ± 1.46	0.11 ± 0.05	1.22 ± 0.19	0.95 ± 0.2	0.83 ± 0.28	2.67 ± 0.25	3.34 ± 0.71

Table S2. CD45$^+$ cell frequencies in the brains of control (PBS) or *T. gondii*-infected mice.

	PMN	Monocytes	T cells	B cells	microglia	NK cells
Mock (early)	0.9 ± 0.26	0.76 ± 0.25	0.48 ± 0.23	0.05 ± 0.04	95.53 ± 0.65	1 ± 0.53
4 DPI	2.02 ± 0.68	1.26 ± 0.82	0.21 ± 0.08	0.01 ± 0.01	94.73 ± 1.76	0.8 ± 0.57
6 DPI	1.09 ± 0.61	2.15 ± 0.71	0.65 ± 0.43	0.05 ± 0.11	93.45 ± 2.96	1.05 ± 0.7
Mock (late)	1.46 ± 0.85	0.76 ± 0.28	0.5 ± 0.12	0.03 ± 0.03	95.62 ± 1.08	0.69 ± 0.27
10 DPI	5.78 ± 1.51	11.38 ± 12.27	3.24 ± 3.42	0.05 ± 0.05	76.96 ± 15.94	1.74 ± 0.39
15 DPI	2.09 ± 2.13	46.61 ± 16.82	19.01 ± 9.4	0.14 ± 0.05	28.16 ± 11	1.05 ± 0.7
38 DPI	1.11 ± 1.01	17.66 ± 2.85	25.73 ± 16.72	0.48 ± 0.39	42.4 ± 17.65	0.69 ± 0.1

Table S3. Antibody panel used for identifying immune cell populations in the blood and the brains of mice.

Antibody Target	Clone	Flourochrome	Company
CCR2	SA203G11	Brilliant Violet 421	Biolegend
Ly6G	1A8	Brilliant Violet 510	Biolegend
NK1.1	PK136	Brilliant Violet 570	Biolegend
CD11b	M1/70	Brilliant Violet 605	Biolegend
CD45	30-F11	APC	Biolegend
CD45	30-F11	Brilliant Violet 785	Biolegend
CD49b	DX5	PE	Biolegend
Ly6C	HK1.4	PerCP-Cy5.5	Biolegend
CD19	6D5	PE-Cy7	Biolegend
CX3CR1	SA011F11	APC	Biolegend
CD3	17A2	APC-Cy7	Biolegend

Table S4. *T. gondii*-infected mouse brain regions significantly ($p < 0.1$) over- or under-represented for monocyte density compared to shuffle analysis.

* This region contains an over-abundance of monocytes compared to the random shuffle; all other regions have fewer monocytes than the random shuffle.

Reference Atlas Region Name	Student's *t* test p-value
Principal mammillary tract	0.0412
Interstitial nucleus of Cajal	0.0917
Anteroventral periventricular nucleus	0.0358
Vascular organ of the lamina terminalis	0.0274
Subparaventricular zone	0.0307
Suprachiasmatic nucleus	0.0552
Periventricular hypothalamic nucleus, preoptic part	0.0256
Anterodorsal preoptic nucleus	0.0557
Tuberomammillary nucleus, dorsal part	0.0219
Anterior hypothalamic nucleus	0.0709
Ventromedial hypothalamic nucleus	0.0307
Ventral premammillary nucleus	0.0540
Accessory supraoptic group	0.0335
Periventricular hypothalamic nucleus, anterior part	0.0219
Arcuate hypothalamic nucleus	0.0335
Periventricular hypothalamic nucleus, intermediate part	0.0833
Medial septal nucleus	0.0557
Olfactory tubercle *	0.0557
Septohippocampal nucleus	0.0358
Claustrum	0.0923
Basolateral amygdalar nucleus, ventral part	0.0599
Ammon's horn	0.0765
Field CA2	0.0846
Field CA1	0.0599
Primary somatosensory area, barrel field, layer 5	0.0656
Primary somatosensory area, barrel field, layer 6a	0.0736
Primary somatosensory area, trunk	0.0450
Primary somatosensory area, trunk, layer 2/3	0.0358
Primary somatosensory area, trunk, layer 5	0.0321
Primary somatosensory area, trunk, layer 6a	0.0736
Primary somatosensory area, trunk, layer 4	0.0256
Primary somatosensory area, upper limb, layer 5	0.0814
Primary somatosensory area, lower limb, layer 5	0.0596

Primary somatosensory area, lower limb, layer 6a	0.0603
Ventral auditory area, layer 5	0.0506
Ventral auditory area, layer 6a	0.0596
Dorsal auditory area, layer 5	0.0844
Posterior auditory area	0.0450
Posterior auditory area, layer 2/3	0.0274
Posterior auditory area, layer 5	0.0358
Posterior auditory area, layer 6b	0.0412
Posterior auditory area, layer 4	0.0450
Posterior auditory area, layer 6a	0.0412
Anterior cingulate area, ventral part, layer 5	0.0666
Agranular insular area, posterior part, layer 2/3	0.0358
Agranular insular area, posterior part, layer 6a	0.0717
Agranular insular area, posterior part, layer 5	0.0420
Perirhinal area	0.0666
Perirhinal area, layer 6b	0.0709
Perirhinal area, layer 5	0.0450
Perirhinal area, layer 6a	0.0557
Perirhinal area, layer 2/3	0.0358
Ectorhinal area	0.0923
Ectorhinal area/Layer 2/3	0.0599
Ectorhinal area/Layer 6a	0.0367
Ectorhinal area/Layer 5	0.0450
Ectorhinal area/Layer 6b	0.0450
Frontal pole, cerebral cortex	0.0335
Frontal pole, layer 2/3	0.0219
Frontal pole, layer 1	0.0358
Anteromedial visual area, layer 2/3	0.0656
Anteromedial visual area, layer 5	0.0889
Anteromedial visual area, layer 4	0.0450
Temporal association areas	0.0599
Temporal association areas, layer 2/3	0.0450
Temporal association areas, layer 5	0.0358
Temporal association areas, layer 6b	0.0666
Temporal association areas, layer 4	0.0358
Temporal association areas, layer 6a	0.0436

Table S5. Regional comparison of monocyte infiltration in the brain during *T. gondii* infection (pink rows) or LPS treatment (blue rows). These data are represented in the volcano plot in Figure 8E.

* Benjamini-Hochberg correction for false discovery rate; $p < 0.1$
† Regions within the reference atlas that could not be reliably assigned to a single brain region

Reference Atlas Region Name	Normalized p value*
Middle cerebellar peduncle	0.0435
Epithalamus related	0.0961
Habenular commissure	0.0369
Basic cell groups and regions	0.0621
Flocculus	0.0550
Lingula (I)	0.0675
Brain stem	0.0849
Midbrain reticular nucleus	0.0418
Interstitial nucleus of Cajal	0.0224
Nucleus of Darkschewitsch	0.0775
Red nucleus	0.0337
Midbrain reticular nucleus, retrorubral area	0.0790
Midbrain, sensory related	0.0822
Inferior colliculus	0.0438
Nucleus ambiguus, ventral division	0.0530
Pontine central gray	0.0636
Tegmental reticular nucleus	0.0377
Interbrain	0.0340
Hypothalamus	0.0199
Periventricular region	0.0512
Anteroventral periventricular nucleus	0.0171
Vascular organ of the lamina terminalis	0.0495
Periventricular hypothalamic nucleus, posterior part	0.0948
Medial preoptic area	0.0381
Suprachiasmatic nucleus	0.0407
Dorsomedial nucleus of the hypothalamus	0.0492
Ventrolateral preoptic nucleus	0.0534
Hypothalamic medial zone	0.0111
Mammillary body	0.0213
Medial mammillary nucleus	0.0148
Tuberomammillary nucleus	0.0223
Tuberomammillary nucleus, ventral part	0.0236
Tuberomammillary nucleus, dorsal part	0.0504
Lateral mammillary nucleus	0.0019

Medial preoptic nucleus	0.0268
Anterior hypothalamic nucleus	0.0494
Ventromedial hypothalamic nucleus	0.0089
Periventricular zone	0.0846
Arcuate hypothalamic nucleus	0.0150
Supraoptic nucleus	0.0351
Periventricular hypothalamic nucleus, intermediate part	0.0759
Hypothalamic lateral zone	0.0456
Zona incerta	0.0700
Fields of Forel	0.0645
Retrochiasmatic area	0.0338
Thalamus, polymodal association cortex related	0.0819
Paraventricular nucleus of the thalamus	0.0798
Epithalamus	0.0321
Lateral habenula	0.0652
Medial habenula	0.0332
Subgeniculate nucleus	0.0487
Intermediodorsal nucleus of the thalamus	0.0386
Peripeduncular nucleus	0.0686
Cerebrum	0.0682
Magnocellular nucleus	0.0868
Medial septal nucleus	0.0220
Striatum ventral region	0.0784
Olfactory tubercle	0.0390
Septohippocampal nucleus	0.0873
Cerebral cortex	0.0788
Claustrum	0.0091
Cortical plate	0.0735
Piriform-amygdalar area	0.0300
Nucleus of the lateral olfactory tract, molecular layer	0.0381
Postpiriform transition area	0.0907
Hippocampal region	0.0809
Field CA1	0.0059
Isocortex	0.0374
Somatomotor areas	0.0559
Primary motor area	0.0242
Primary motor area, Layer 2/3	0.0493
Primary motor area, Layer 6a	0.0037
Primary motor area, Layer 1	0.0816
Primary motor area, Layer 5	0.0414
Secondary motor area, layer 6a	0.0390

Secondary motor area, layer 6b	0.0617
Somatosensory areas	0.0102
Unlabeled†	0.0023
Unlabeled†	0.0179
Unlabeled†	0.0198
Primary somatosensory area	0.0065
Primary somatosensory area, barrel field	0.0319
Primary somatosensory area, barrel field, layer 2/3	0.0930
Primary somatosensory area, barrel field, layer 5	0.0040
Primary somatosensory area, barrel field, layer 6a	0.0327
Primary somatosensory area, barrel field, layer 4	0.0145
Primary somatosensory area, mouth	0.0054
Primary somatosensory area, mouth, layer 2/3	0.0019
Primary somatosensory area, mouth, layer 5	0.0067
Primary somatosensory area, mouth, layer 6a	0.0766
Primary somatosensory area, mouth, layer 4	0.0014
Primary somatosensory area, trunk	0.0002
Primary somatosensory area, trunk, layer 2/3	0.0030
Primary somatosensory area, trunk, layer 5	0.0018
Primary somatosensory area, trunk, layer 6a	0.0658
Primary somatosensory area, trunk, layer 4	0.0000
Primary somatosensory area, nose, layer 5	0.0725
Primary somatosensory area, upper limb	0.0640
Primary somatosensory area, upper limb, layer 5	0.0044
Primary somatosensory area, upper limb, layer 1	0.0912
Primary somatosensory area, lower limb	0.0064
Primary somatosensory area, lower limb, layer 2/3	0.0268
Primary somatosensory area, lower limb, layer 5	0.0282
Primary somatosensory area, lower limb, layer 1	0.0018
Primary somatosensory area, lower limb, layer 6a	0.0036
Gustatory areas	0.0544
Gustatory areas, layer 2/3	0.0295
Gustatory areas, layer 1	0.0432
Primary auditory area, layer 5	0.0916
Primary auditory area, layer 4	0.0153
Ventral auditory area	0.0325
Ventral auditory area, layer 5	0.0013
Ventral auditory area, layer 4	0.0972
Ventral auditory area, layer 1	0.0980
Ventral auditory area, layer 6a	0.0208
Dorsal auditory area	0.0783

Dorsal auditory area, layer 5	0.0034
Dorsal auditory area, layer 4	0.0794
Posterior auditory area	0.0651
Posterior auditory area, layer 2/3	0.0343
Posterior auditory area, layer 5	0.0637
Posterior auditory area, layer 6a	0.0384
Anterior cingulate area, dorsal part, layer 6a	0.0468
Anterior cingulate area, ventral part	0.0249
Anterior cingulate area, ventral part, layer 2/3	0.0407
Anterior cingulate area, ventral part, layer 6a	0.0174
Anterior cingulate area, ventral part, layer 5	0.0397
Anterior cingulate area, ventral part, layer 6b	0.0040
Agranular insular area, posterior part	0.0022
Agranular insular area, posterior part, layer 2/3	0.0217
Agranular insular area, posterior part, layer 1	0.0016
Agranular insular area, posterior part, layer 5	0.0102
Retrosplenial area, lateral agranular part, layer 6b	0.0469
Perirhinal area	0.0014
Perirhinal area, layer 6b	0.0064
Perirhinal area, layer 5	0.0086
Perirhinal area, layer 6a	0.0047
Perirhinal area, layer 2/3	0.0027
Perirhinal area, layer 1	0.0153
Ectorhinal area	0.0040
Ectorhinal area/Layer 2/3	0.0129
Ectorhinal area/Layer 6a	0.0357
Ectorhinal area/Layer 5	0.0489
Ectorhinal area/Layer 1	0.0053
Ectorhinal area/Layer 6b	0.0813
Unlabeled[†]	0.0045
Frontal pole, cerebral cortex	0.0082
Frontal pole, layer 2/3	0.0050
Frontal pole, layer 1	0.0122
Anteromedial visual area	0.0560
Anteromedial visual area, layer 2/3	0.0320
Anteromedial visual area, layer 5	0.0075
Anteromedial visual area, layer 4	0.0394
posteromedial visual area, layer 2/3	0.0928
posteromedial visual area, layer 4	0.0235
Anterolateral visual area, layer 5	0.0383
Anterolateral visual area, layer 4	0.0620

Unlabeled[†]	0.0002
Temporal association areas	0.0096
Temporal association areas, layer 2/3	0.0195
Temporal association areas, layer 5	0.0030
Temporal association areas, layer 4	0.0414
Temporal association areas, layer 1	0.0679
Temporal association areas, layer 6a	0.0277
Orbital area, lateral part, layer 5	0.0659

Movie S1. Monocyte motility at the BBB in a *T. gondii*-infected mouse at 4 dpi. A representative video of a CCR2$^{RFP/+}$ mouse at 4 dpi with *T. gondii.* The brain was imaged through a cranial window using two-photon microscopy. Gray lines were added to outline the major vessels in the FOV (note: not all vessels were outlined).

Movie S2. Monocyte motility at the BBB in a *T. gondii*-infected mouse at 15 dpi. A representative video of a CCR2$^{RFP/+}$ mouse at 15 dpi with *T. gondii.* The brain was imaged through a cranial window using two-photon microscopy. Gray lines were added to outline the major vessels in the FOV (note: not all vessels were outlined).

Movie S3. Analysis and registration pipeline for CCR2$^{RFP/+}$ mice. A representative imaging dataset of CCR2-RFP cells from CCR2$^{RFP/+}$ mice infected with *T. gondii.* Monocyte data were warped into the Allen reference atlas using autofluorescence information. The density of detected cells registered to the atlas were converted to heatmaps and shown for five different infected mice and for the mean distribution across the five replicates.

Supplementary Materials and Methods

Mouse Experiments

Wild-type C57BL/6J and $CCR2^{RFP/RFP}$ mice were purchased from Jackson Labs. $CCR2^{+/RFP}$ mice were bred in-house using homozygous $CCR2^{RFP/RFP}$ mice and WT C57BL/6J mice. $CCR2^{+/RFP}CX3CR1^{+/GFP}$ double reporter mice were bred in-house by crossing homozygous reporter mice (a gift from Dr. Andrea Tenner) with WT C57BL/6J mice.

Serum Cytokine Multiplex Assay

Blood was isolated from anesthetized mice prior to perfusion and stored in coagulation tubes (BD Biosciences, San Jose, CA). Serum was isolated from coagulated blood by centrifugation per the manufacturer's recommendations and stored at -80°C. Cytokines were measured using the LegendPlex bead-based assay (Biolegend, San Diego, CA) per the kit instructions at a dilution of 1:2. Samples were analyzed on a Novocyte flow cytometer (Acea Biosciences, San Diego, CA).

Immunofluorescence Imaging

For antibody staining, sections were rinsed in PBS for 1-2 min, and blocked and permeabilized in IFA buffer [1X PBS (Corning), 5% normal goat serum (Southern Biotech, Birmingham, AL), 0.3% Triton-x 100 (Thermo Fisher Scientific)] for 2-4 hr. Antibodies against collagen IV (1:500; Abcam, Cambridge, MA), Glut-1 (1:500; Millipore), IBA-1 (1:500; WAKO), RFP (1:400; Rockland), or CST-1 (1:200 a gift from Dr. Louis Weiss (1) were diluted in IFA buffer and incubated with sections for 16 hr (anti-CST-1, IBA-1, and RFP) or 48 hr (Glut-1, collagen IV). Following washes in 1X PBS, secondary antibodies were diluted at 1:500 in IFA buffer and

incubated with sections for 24 hr. Nuclei were stained just prior to the final wash using Hoechst dye (1:20,000; Sigma).

Microglia and RFP$^+$ Cell Quantification

Microglia were quantified using the Spot counting function in Imaris on 20x magnification confocal images from CCR2$^{+/RFP}$CX3CR1$^{+/GFP}$ reporter mice infected with *T. gondii*. At least 18 individual fields of view within the isocortex were selected in two independent brain sections per animal. Threshold values for quantification were determined for RFP and GFP channels by visual inspection to ensure that cells were counted accurately. In addition, GFP channel threshold values were selected that only included cells with microglia morphology and high GFP expression to mitigate counting of GFP^{lo} cells.

Fixed Tissue Apoptosis Staining

Fixed brain tissue sections (25 μm) were removed from cryopreservation media and blocked, permeabilized, and stained with anti-RFP antibody, as described above. After staining, sections were treated per the kit instructions of the TUNEL Andy Flour 647 Apoptosis Detection kit (GeneCopoeia, Rockville, MD). DNase was applied for 20 minutes to tissue sections generate to positive control data, and nuclei were counterstained with Hoechst (1:20,000; Sigma). Sections were imaged at 20x magnification on a Leica SP8 microscope and quantified using FIJI software (NIH). Each image was divided into 180 μm squares to facilitate quantification, and thresholding was applied to each channel to isolate signal and measure field area covered. For TUNEL quantification, a mask was created using the nuclear signal, and the area of 647 nm signal within the mask was measured.

Cranial Window Implantation

Mice were anesthetized with isoflurane in O_2 (2% for induction, 1-1.5% for maintenance, Patterson Veterinary, Devens, MA). To provide systemic and local perioperative analgesia, Carprofen (10 mg/kg, s.c., Zoetis) and topical 2% lidocaine hydrochloride jelly (Akorn, Lake Forest, IL) were administered, respectively. Ringer's lactate solution (0.2 mL/20 g/hr, s.c.) was given to replace fluid loss. Sterile eye ointment (Rugby, Livonia, MI) was used to prevent corneal drying. All surgical tools were sterilized using a hot glass bead sterilizer (Germinator 500). Following sterilization with Povidone-iodine, the scalp and underlying connective tissue were removed to expose the parietal and interparietal bone, and the right temporal muscle was detached from the superior temporal line. The skull was dried using ethanol (70% in DI water) and a thin layer of the tissue adhesive Vetbond (3M) was applied. Custom-printed ABS headplates were attached using the acrylic resin Ortho-Jet BCA (Lang Dental, Wheeling, IL) at an angle parallel to the skull. A small craniotomy (3 mm) was performed over the right hemisphere 2.5 mm anterior and 3 mm lateral lambda. GELFOAM sterile sponges (Patterson Veterinary) pre-soaked in sterile saline were used to absorb bleeding from the dura. Surgery was terminated if dural tears or parenchymal bleeding was observed (1 of 11 mice). A 4 mm glass coverslip (World Precision Instruments, Sarasota, FL) was placed over the exposed brain and pressed against thinned bone surrounding the craniotomy, and the edges were affixed to the skull first with a thin layer of Vetbond and second with acrylic resin. Following surgery, mice recovered in their home cage over a warm heating pad until normal behavior resumed (~15-30 min). Post-operative care consisted of daily Carprofen injections (10 mg/kg, s.c.) for at least 4 days following surgery, ending at least 1 day prior to two-photon imaging. Mice with post-operative bleeding (2 of 11 mice) were excluded from the study.

Blinding

Blinding was done for the two-photon microscopy experiments. The researcher who performed craniotomies was blinded as to whether the mice would be subsequently injected with PBS (control group) or with *T. gondii* (infected group). In addition, the researcher who performed the two-photon imaging was blinded as to whether the mice being imaged were control or infected mice.

Two-Photon Image Processing

During two-photon imaging, autofluorescent particles in both the red and green channels (thought to be lipofuscin inclusions) were detected. To visualize the red fluorescence specific to monocytes, ratiometric images on a per pixel basis were generated using the Image Calculator function in FIJI, followed by adjustment of the brightness applied equally across the entire image. For quantification of monocyte accumulation, RFP area was quantified by thresholding every image using the same upper limit value for every mouse and using the Measure function in FIJI.

Whole Brain Cell Segmentation Analysis

For cell detection, a pixel classifier was trained in ilastik on a subset of $CCR2^{RFP/+}$ imaging data from a *T. gondii*-infected mouse at 15 dpi (2). The classifier was applied to the five $CCR2^{RFP/+}$ mice infected with *T. gondii* and four LPS-injected mice. For LPS datasets the classifier had a slight modification made to maintain the same behavior while accounting for the different conditions. Segmented cells were extracted from the output probability mask output using ilastik's built-in identity-preserving hysteresis thresholding with the following parameters:

sigmas= 1,1,1, size range= 8, 1000000, thresholds= 0.2, 0.7. Cell coordinates were defined as the local maxima within segmented cells. Using alignment procedures previously described (3), cytoarchitectural autofluorescence signal was used to locate cell coordinates in the annotated Allen reference atlas, version 2 (http://alleninstitute.org/). Unlike the original ClearMap release, Advanced Neuroimaging Tools (ANTs) was used for registration (4). Despite the propensity of the iDISCO$^+$ protocol to quench fluorescent proteins, we noted intact GFP fluorescence from the *T. gondii* in the autofluorescence channel. The GFP signal did not affect the quality of registration. Chromatic aberration correction was done using an affine registration between the autofluorescence and CCR2-RFP channels and applied to detected cell coordinates. Alignment to the Allen atlas was done using sequential rigid, affine, and symmetric normalization algorithms that were applied to cells. Cells were then assigned to voxels in the lower-resolution (25 μm^3) reference atlas and given a region designation based on the voxel location in the annotated atlas. Given the hierarchical structure of the atlas, parent regions inherited the cell counts and volume of their children. Due to dissection inconsistencies, main olfactory bulb, accessory olfactory bulb, anterior olfactory nucleus, olfactory nerve, and optic chiasm were excluded from analysis. Individual and mean heatmaps were generated using ClearMap. Example images were passed through a 3-pixel wide median filter to reduce camera noise, and the intensity was matched between *T. gondii*-infected, LPS and PBS control groups.

Validation of Cell Detection and Segmentation

Two independent raters not involved in classifier training manually counted RFP$^+$ cells in a representative 3D substack of the classifier training using FIJI (5). Due to variability in approximating cell centers, correlation between raters and classifier was determined by taking

the sum of detected cells within spatial bins representing cubic volumes with 10, 20, 30, 40, and 50 voxels per side across the image. For each bin size, the Pearson correlation was calculated for the binned cell distribution between raters.

Statistical Methods

For flow cytometry experiments, cytokine multiplex, and monocyte accumulation data comparing multiple groups, one-way ANOVA with Tukey post-hoc test was used. $CCR2^{RFP/+}CX3CR1^{GFP/+}$ monocyte frequencies were evaluated using a two-tailed Student's *t* test. Changes in monocyte speed and motility mode were evaluated by comparing the linear regression curves over the time-course and testing for differences in slope by two-tailed student's *t* test. Similarly, weight loss was evaluated by comparing slopes of linear regression analysis applied to portions of the weight loss curves and testing for differences between wild-type C57BL/6J mice and $CCR2^{RFP/+}CX3CR1^{GFP/+}$ reporter mice using a Student's *t* test. Kaplan-Meier survival curves were compared using a log-rank test (Graphpad Prism) $*p < 0.05$; $**p < 0.01$; $***p < 0.001$.; $****p < 0.0001$. All error bars are given as the standard error of the mean unless otherwise indicated. Graphs were generated using Graphpad Prism or coded using R software and the ggplot2 package(6, 7) .

Statistical analysis of monocyte distribution was done using custom python scripts (Python Software Foundation, https://www.python.org/). To compare the distribution of monocytes against random chance, cells from each animal were first placed into the reference atlas at 25 μm^3 voxel resolution. Voxels, with their associated cell counts, were shuffled 1000 times for each animal. The median cell count by region calculated from the shuffle procedure was used to estimate the random chance level of monocyte density. A two-tailed Student t-test

with Benjamini-Hochberg correction (alpha=0.1) was performed on cell densities of experimental and shuffled groups for each region. Standard deviation and mean across animals for both groups was also calculated. For comparison of the *T. gondii* and LPS conditions, a two-tailed Student t-test with Benjamini-Hochberg correction (alpha=0.1) was performed for each region between the two groups.

References

1. Tomita T*, et al.* (2013) The Toxoplasma gondii cyst wall protein CST1 is critical for cyst wall integrity and promotes bradyzoite persistence. *PLoS Pathogens* 9(12):e1003823.
2. Sommer C, Strahle C, Köthe U, & Hamprecht FA (2011) ilastik: Interactive Learning and Segmentation Toolkit. *Eigth IEEE International Symposium on Biomedical Imaging (ISBI).* pp 230-233.
3. Renier N*, et al.* (2016) Mapping of Brain Activity by Automated Volume Analysis of Immediate Early Genes. *Cell* 165(7):1789-1802.
4. Avants BB*, et al.* (2011) A reproducible evaluation of ANTs similarity metric performance in brain image registration. *NeuroImage* 54(3):2033-2044.
5. Schindelin J*, et al.* (2012) Fiji: an open-source platform for biological-image analysis. *Nature Methods* 9(7):676-682.
6. Wickham H (2009) *ggplot2: Elegant Graphics for Data Analysis* (Springer-Verlag New York) p 213.
7. Team RC (2013) R: A Language and Environment for Statistical Computing (R Foundation for statistical Computing Vienna, Austria), 3.3.3 (2017-03-06).